# Fiber–Particle Composite Binder Enabled Feasibly Dry-Processed Ultrahigh-Nickel Cathode Film for All-Solid-State Lithium Batteries

Ye-Chao Wu, Xiao-Bin Cheng, Feng Li, Hao-Yuan Tan, Xin Huang, Jin-Da Luo, Shu Chen, Ruijun Pan, Yi-Chen Yin,* and Hong-Bin Yao*

Cathodes play a critical role in determining the performance of all-solid-state lithium batteries (ASSLBs). Traditional dry-processed cathode based on only fibrous binder suffers from limited binder fibrillation and loose contact between solid particles inside. Herein, a fiber-particle composite binder is employed to fabricate a dry-processed cathode comprising single-crystal $LiNi_{0.92}Co_{0.05}Mn_{0.03}O_2$ (S-NCM92) and $Li_3InCl_6$ (LIC). The incorporation of 1.5 wt% polytetrafluoroethylene (PTFE) particles and 1 wt% PTFE fibers promotes interparticle contact, thereby enhancing the mechanical adhesion among solid components.

As the result, the optimized dry-processed cathode shows a marked improvement in rate capability and cycling stability. Moreover, the dry-processed cathode with fiber-particle composite binder enables a pouch cell with a capacity of 10.89 mAh to exhibit 68.8% capacity retention after 80 cycles under a stack pressure of 31.25 MPa. The cell maintains electrochemical function after cutting, demonstrating its safety and reliability. These results underscore the practicality of the fiber-particle composite binder strategy to fabricate high-quality cathodes for ASSLBs.

## 1. Introduction

All-solid-state lithium batteries (ASSLBs) are promising to relieve the safety concerns of commercial lithium-ion batteries and meanwhile deliver higher energy density.[1–4] However, most studies on ASSLBs have primarily focused on laboratory-scale mold cells assembled with electrode-adhered solid electrolyte (SE) pellets by cold-pressed under high pressure (>300 MPa), which are incompatible with continuous electrode film fabrication required in practical applications.[5–7] The quality of electrode film, governed by the properties of the solid electrolyte and film-formation process, is central to constructing durable ASSLBs. Among various solid electrolytes, chloride SEs have emerged as promising catholytes[8–10] owing to their wide electrochemical window, sufficient deformability, and high ionic conductivity.[11–14] They can well match ternary layered cathode materials with high voltage and large capacity (e.g., $LiNi_{0.92}Co_{0.05}Mn_{0.03}O_2$),[15] enabling high-performance chloride

SEs-based ASSLBs.[16] While wet slurry technique is widely used for electrode fabrication,[17] the solvent sensitivity of chloride SEs (e.g., $Li_3InCl_6$) precludes conventional wet-slurry processing, as exposure to polar solvents degrades ionic conductivity.[18–20] Consequently, solvent-free dry processing emerges as a critical alternative to maintain the integrity of chloride SEs during cathode fabrication.[21] However, previously reported dry-processed cathode films that relied solely on fibrous binders suffered from uneven material distribution, insufficient binder fibrillation, and poor film quality, ultimately compromising the electrochemical performances of the as-fabricated ASSLBs. So it is essential to investigate more appropriate contents, sizes, and types of the PTFE binders.[22]

Herein, we employed 1.5 wt% particulate and 1 wt% fibrous PTFE to facilitate the fibrillation of binder for the dry-processed cathode. Compared with the dry-processed cathode with only PTFE fibers, the optimized dry-processed cathode exhibits a significant improvement in rate performance, with delivered specific capacity increasing from 85.9 to 98.6 mAh g$^{-1}$ at 1.0 C. Furthermore, the capacity retention after 100 cycles increases from 64.7% (96.9 mAh g$^{-1}$) to 76.3% (115.3 mAh g$^{-1}$). To demonstrate the scalability, a pouch cell using the optimized dry-processed cathode was assembled, which retained 68.8% capacity after 80 cycles at 0.2 C and remained operational after mechanical damage, successfully powering an LED bulb. The fiber–particle composite binder strategy facilitates the formation of a robust, scalable, and damage-tolerant cathode, thereby advancing the practical development of ASSLBs.

## 2. Results and Discussion

**Figure 1**a–c schematically illustrates the preparation process of the dry-processed composite cathode. As shown in Figure 1a,

Y.-C. Wu, X.-B. Cheng, J.-D. Luo, Y.-C. Yin, H.-B. Yao
Department of Applied Chemistry
University of Science and Technology of China
Hefei, Anhui 230026, China
E-mail: artist@ustc.edu.cn
        yhb@ustc.edu.cn

F. Li, H.-Y. Tan, Y.-C. Yin, H.-B. Yao
Hefei National Research Center for Physical Sciences at the Microscale
University of Science and Technology of China
Hefei, Anhui 230026, China

X. Huang, S. Chen, R. Pan
Department of Frontier Technology
Hefei Gotion High-tech Power Energy Co., Ltd.
Hefei, Anhui 230012, China
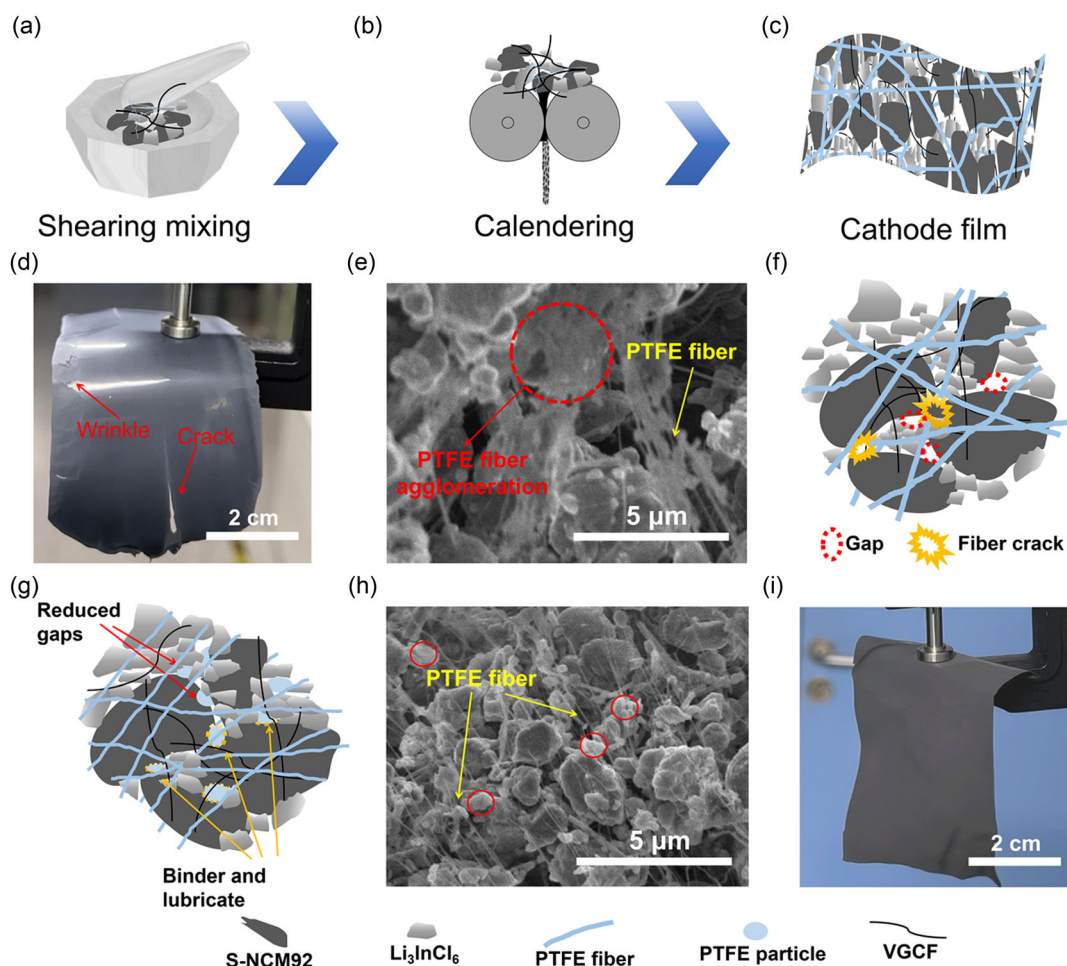
**Figure 1.** Dry-processed cathode and formation mechanism. (a–c) Schematic of the preparation of dry-processed cathode: a) shear mixing, b) roller pressing, and c) formation of the composite cathode film. d) Photograph of a conventional $P_0F_1$ dry-processed composite cathode film. e) SEM image of a $P_0F_1$ dry-processed composite cathode. f) Schematic illustration of the internal structure of a dry-processed composite cathode using only fibrous PTFE as the binder. g) Schematic illustration of the internal structure of a fiber-particle composite binder-based dry-processed cathode. h) SEM image of a $P_{1.5}F_1$ dry-processed composite cathode. The PTFE fibers are marked by yellow arrows and the PTFE particles are marked by red cycles. i) Photograph of the optimized $P_{1.5}F_1$ dry-processed composite cathode film.

single-crystal $LiNi_{0.92}Co_{0.05}Mn_{0.03}O_2$ (S-NCM92) cathodes, $Li_3InCl_6$ solid electrolytes (LIC), polytetrafluoroethylene (PTFE) binders, and vapor-grown carbon fiber (VGCF) conductive agents were manually mixed and ground in a mortar. Then the powder mixture was calendared multiple times using a roller press (Figure 1b) to form a continuous and flexible composite cathode (Figure 1c). The dry-processed composite cathode with only 1 wt% PTFE fibers as binder (denoted as $P_0F_1$) often results in poor film quality with cracks and wrinkles (indicated by the red arrows in Figure 1d). Scanning electron microscopy (SEM) image in Figure 1e indicates localized agglomeration of PTFE arising from its insufficient fibrillation inside cathodes. Additionally, due to the inherent rigidity of S-NCM92 particles, the sliding motion of active material particles during the dry roll-pressing process generates shear stress, which can easily cause the fractures of fibrillated PTFE (indicated by the yellow starburst shapes in Figure 1f). As a result, gaps forming at the contact edges of S-NCM92 particles (outlined in red dashed circles in Figure 1f), leading to brittleness of the cathode film and thereby hindering ion/electron transport inside. To reduce the gaps and enhance

the contact between solid components in the dry-processed composite cathode (red and yellow arrows in Figure 1g), we added an additional 1.5 wt% of PTFE particles, which are uniformly dispersed in the dry-processed composite cathode (red circles in Figure 1h). This sample is labeled as $P_{1.5}F_1$. The self-lubricating nature of the PTFE particles increases the fibrillation degree of PTFE fibers and thus improves the dispersion of well-fibrillated PTFE fibers (yellow arrows in Figure 1h) and other solid components, thereby facilitating high-quality composite film formation (Figure 1i) and promoting ion/electron conduction within the dry-processed composite cathode.

Electrochemical performances of $P_0F_1$ and $P_{1.5}F_1$ are compared to evaluate the effects of PTFE particle addition, while the composite cathode sample without any PTFE binders (comprising only S-NCM92, LIC, and VGCF, denoted as $P_0F_0$) serves as a reference to illustrate the intrinsic discharge capacity of S-NCM92. It should be noted that $P_0F_0$ was prepared by powder cold-pressing because it cannot self-support as a film, while $P_0F_1$ and $P_{1.5}F_1$ were directly cut from the dry-processed films as shown in Figure 1d and i. All-solid-state mold cell was assembled

**Batteries & Supercaps**

Research Article
doi.org/10.1002/batt.202500375

**Chemistry
Europe**

European Chemical
Societies Publishing

using InLi alloy as the anode and sulfide electrolyte ($Li_6PS_5Cl$) as the protective layer to minimize anode interference for the evaluation (**Figure 2**a). Under the rate of 0.05 C at 30 °C, the initial discharge capacities of the $P_0F_0$, $P_0F_1$, and $P_{1.5}F_1$ samples were 236.7, 226.7, and 231.1 mAh g$^{-1}$, respectively, with corresponding coulombic efficiencies of 95.9%, 94.0%, and 94.7% (Figure 2b). Local dispersion inhomogeneity in $P_0F_1$ as shown in Figure 1e hinders the electrochemical performance of the active S-NCM92, resulting in lower initial discharge capacity and coulombic efficiency. In contrast, the extra addition of 1.5 wt% PTFE particles helps achieve uniform dispersion of PTFE fibers (Figure 1h), promoting contact between components for ion-electron transport in the composite cathode. It should be noted that both PTFE particles and fibers are electrochemically inert, thus leading to slightly lower specific capacities of $P_0F_1$ and $P_{1.5}F_1$ than PTFE-free $P_0F_0$. As shown in the corresponding dQ/dV curves, $P_0F_0$, $P_0F_1$, and $P_{1.5}F_1$ all exhibit three distinct phase transition peaks (Figure 2c): a transition from hexagonal to monoclinic phase

(H1→M) at 3.60 V, a transition from monoclinic to another hexagonal phase (M→H2) at ~4.0 V, and a transition between two hexagonal phases (H2→H3) at 4.18 V.[23–25]

At low current densities, the dQ/dV curves for $P_0F_0$, $P_0F_1$, and $P_{1.5}F_1$ show good overlap of areas and characteristic peaks, indicating that the presence or absence of PTFE has negligible impact on the overall performance of the composite cathodes during initial low-rate charge/discharge in the mold cell under high external pressure. However, PTFE addition improves capacity retention of composite cathodes under higher cycling rates (Figure S1, Supporting Information). The rate performances at 0.1, 0.2, 0.3, 0.5, and 1.0 C for $P_0F_0$, $P_0F_1$, and $P_{1.5}F_1$ were shown in Figure 2d,e,f and Table S1, Supporting Information, respectively. From the charge–discharge curves, the $P_0F_0$ sample shows a sharp decline in capacity from 227.1 mAh g$^{-1}$ at 0.1 C to 50.5 mAh g$^{-1}$ at 1.0 C, with a capacity retention of only 22.2%. In contrast, the $P_0F_1$ and $P_{1.5}F_1$ cathodes exhibit higher discharge capacities of 85.9 and 98.6 mAh g$^{-1}$ at 1.0 C. The discharge
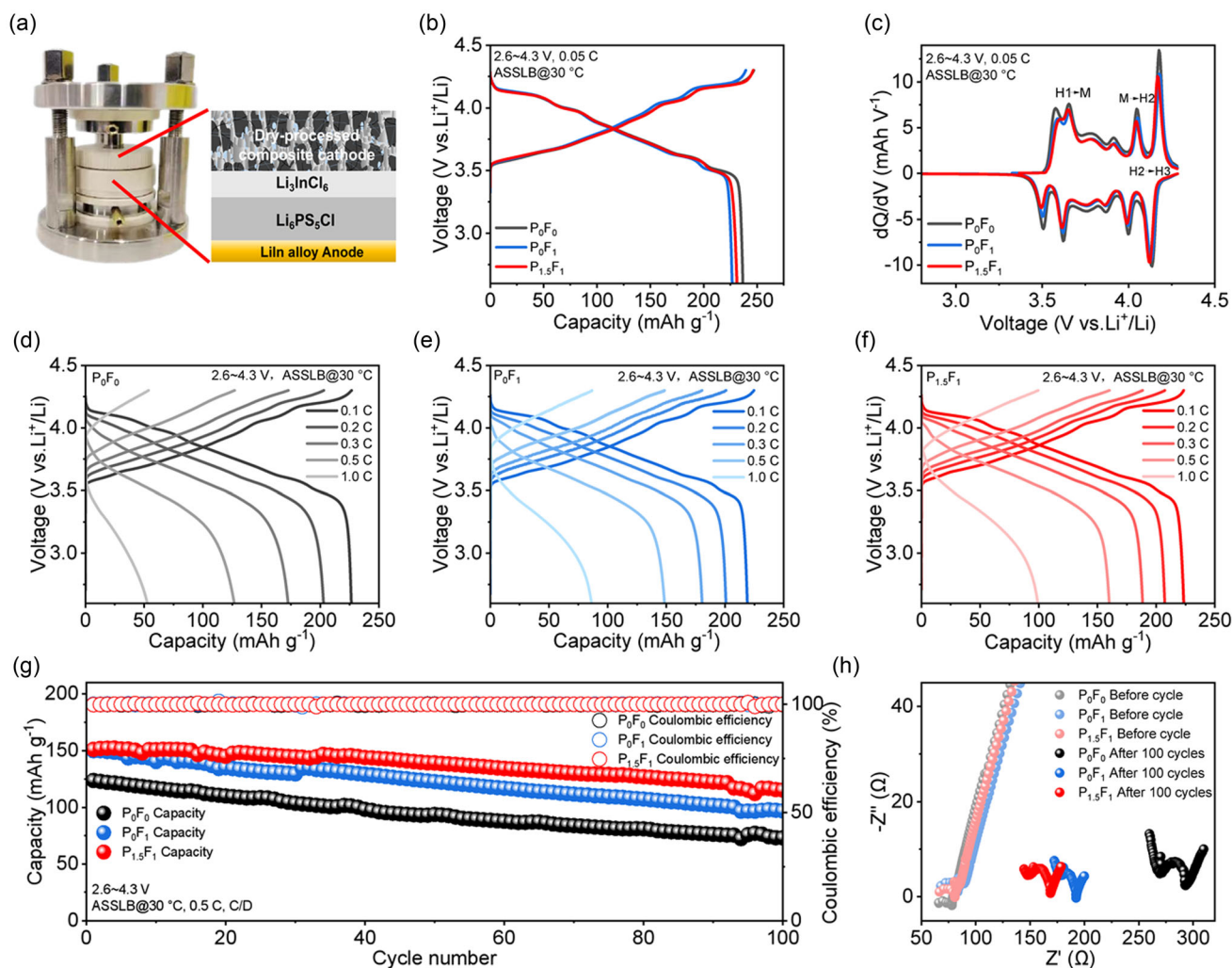


**Figure 2.** Electrochemical characterization of dry-processed composite cathodes. a) Schematic of the assembled all-solid-state mold cell unit. b) Initial charge–discharge curves of dry-processed composite cathodes $P_0F_0$, $P_0F_1$, and $P_{1.5}F_1$. c) Corresponding dQ/dV curves for the initial charge-discharge voltage curves of $P_0F_0$, $P_0F_1$, and $P_{1.5}F_1$. d–f) Charge–discharge voltage curves of $P_0F_0$, $P_0F_1$, and $P_{1.5}F_1$ dry-processed composite cathodes at rates of 0.1, 0.2, 0.3, 0.5, and 1.0 C. (g) Cycle performances of $P_0F_0$, $P_0F_1$, and $P_{1.5}F_1$ dry-processed composite cathodes at 0.5 C. (h) EIS spectra of ASSLBs based on $P_0F_0$, $P_0F_1$, and $P_{1.5}F_1$ dry-processed composite cathodes before and after 100 cycles. The areal capacity of $P_0F_0$, $P_0F_1$, and $P_{1.5}F_1$ is ~3 mAh cm$^{-2}$.

**Batteries & Supercaps**

Research Article
doi.org/10.1002/batt.202500375

**Chemistry Europe**
European Chemical
Societies Publishing

voltage plateau drop of $P_0F_0$ is the largest, with the median voltage decreasing from 3.21 V to 2.55 V, exhibiting the greatest polarization (Figure 2d). For $P_0F_1$ the median voltage drops from 3.23 V to 2.69 V, with a capacity retention of 39.2% at 1.0 C (Figure 2e). It is rewarding that $P_{1.5}F_1$ shows the smallest discharge voltage plateau drop with the median voltage decreasing from 3.67 V to 3.32 V and its capacity retention is up to 44.2% at 1.0 C (Figure 2f), indicating better ion/electron transport inside. It is further confirmed by direct current polarization tests (Figure S2, Supporting Information), which showed that the ionic conductivity of the $P_0F_1$ sample is $3.1 \times 10^{-3}$ mS cm$^{-1}$, while the $P_{1.5}F_1$ sample has a slightly higher value of $4.1 \times 10^{-3}$ mS cm$^{-1}$ (Figure S2a, Supporting Information). The electronic conductivities of $P_0F_1$ and $P_{1.5}F_1$ are 0.26 mS cm$^{-1}$ and 0.35 mS cm$^{-1}$, respectively (Figure S2b, Supporting Information). These results suggest that the enhanced solid–solid contact inside the cathode facilitates electronic and ionic conduction.

Long-cycling tests of all cathodes were further conducted at a rate of 0.5 C. As shown in Figure 2g, the capacity retention for $P_0F_0$, $P_0F_1$, and $P_{1.5}F_1$ at 100th cycle are 59.0, 64.7, and 76.3%, respectively. According to the cycling data of the all-solid-state mold battery using the $P_0F_0$ sample (Figure S3a, Supporting Information), in the initial five cycles, the voltage at 50% depth of discharge drops from 3.46 to 3.44 V, and the discharge capacity decreases from 123.0 mAh g$^{-1}$ to 120.9 mAh g$^{-1}$. At the 100th cycle, the voltage plateau decreases by an additional 280 mV (voltage plateau at only 3.18 V), and the polarization in the charge–discharge curve become more pronounced (Figure S3a, Supporting Information). The corresponding dQ/dV charging curve also shows less distinct phase transition peaks (Figure S3b, Supporting Information), where the first phase transition peak of the dQ/dV charging curve shifts from 3.82 V (at the first cycle) to 3.94 V (at the 100th cycle). For $P_0F_1$, the discharge curves show clear discharge voltage plateau in the first five cycles (Figure S3c, Supporting Information), but after 100 cycles, the voltage at 50% depth of discharge dropped from 3.58 to 3.31 V. From the dQ/dV charging curve (Figure S3d, Supporting Information), it can be observed that the first phase transition peak shifts from 3.77 V (at the first cycle) to 3.90 V (at the 100th cycle). For $P_{1.5}F_1$, the discharge curve exhibits
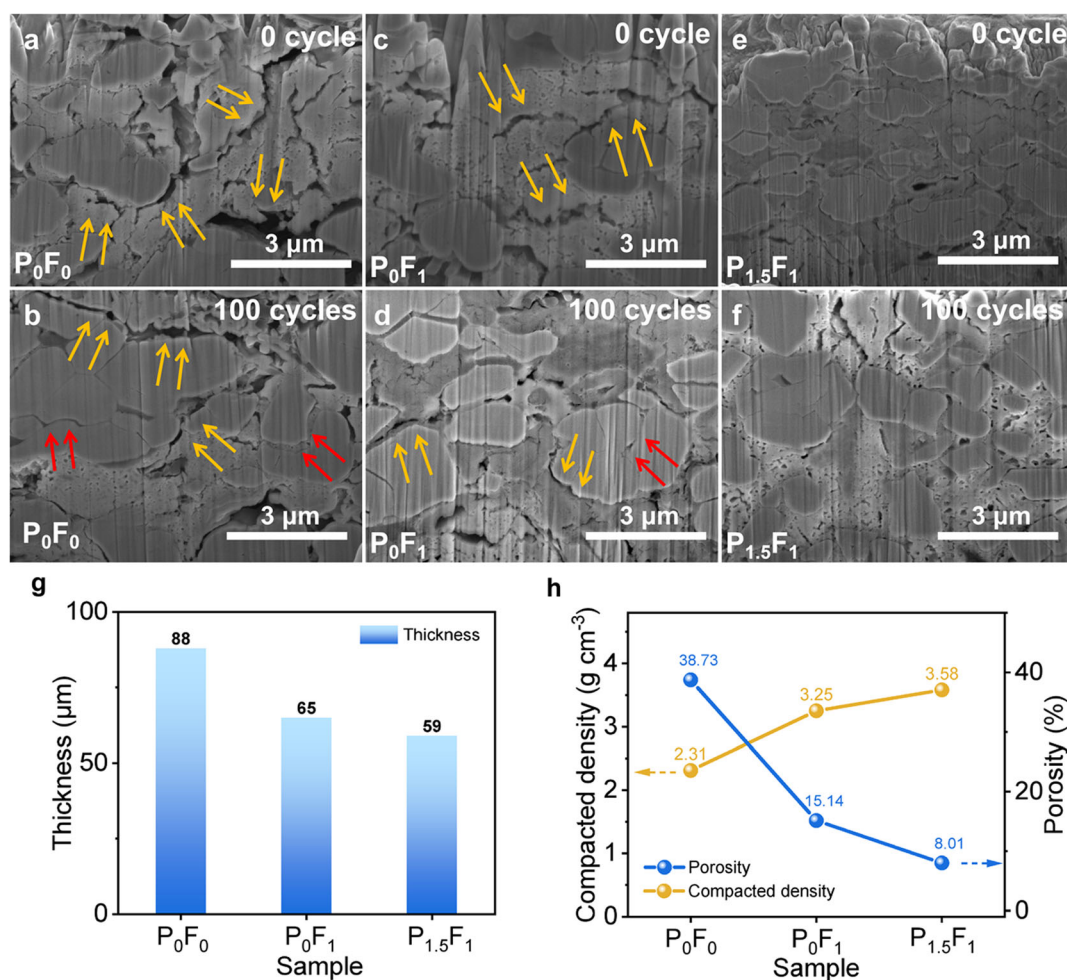


**Figure 3.** Evolution of physical contact during the cycling process of $P_0F_0$, $P_0F_1$, and $P_{1.5}F_1$ dry-processed composite cathodes. a,b) FIB-SEM images of the $P_0F_0$ dry-processed composite cathode before and after 100 cycles. c,d) FIB-SEM images of the $P_0F_1$ dry-processed composite cathode before and after 100 cycles. e,f) FIB-SEM images of the $P_{1.5}F_1$ dry-processed composite cathode before and after 100 cycles. g) Thickness changes of $P_0F_0$, $P_0F_1$, and $P_{1.5}F_1$ dry-processed composite cathodes after compaction at 400 MPa. h) Calculations of the compaction density and porosity of $P_0F_0$, $P_0F_1$, and $P_{1.5}F_1$ dry-processed composite cathodes.

**Batteries & Supercaps**

Research Article
doi.org/10.1002/batt.202500375

**Chemistry Europe**
European Chemical
Societies Publishing

a more pronounced discharge plateau voltage during the first five cycles (Figure S3e, Supporting Information). After 100 cycles, the voltage at 50% discharge state decreases from 3.57 V (at the first cycle) to 3.39 V, with a plateau voltage reduction of only 180 mV. From the dQ/dV charging curve (Figure S3f, Supporting Information), it can be observed that the first phase transition peak shifts from 3.82 V (in the first cycle) to 3.94 V (at the 100th cycle). These electrochemical results further validate the reliability of our experimental design (Figure 1). We further tested the EIS curves before and after cycling (Figure 2 h). Before cycling, $P_0F_0$, $P_0F_1$, and $P_{1.5}F_1$ all-solid-state mold cells display similar impedances of ~80 Ω. After 100 cycles, the impedance of $P_0F_0$ increases to 292.9 Ω, while those of $P_0F_1$ and $P_{1.5}F_1$ only increase to 192.3 and 168.7 Ω, respectively. Since the SE and active materials in the three composite cathodes have the same composition, the byproducts generated at the interface during cycling would be very similar, including InClO and $In_2O_3$.[26]

To identify the mechanisms underlying the improvement of the composite cathode's mechanical properties or interfacial contact during cycling, we performed focused ion beam-scanning electron microscope (FIB-SEM) characterization on the $P_0F_0$, $P_0F_1$, and $P_{1.5}F_1$ composite cathodes to observe their internal morphology evolutions before and after 100 cycles (**Figure 3**). For the $P_0F_0$ sample, the interparticle contact inside before cycling is poor with obvious gaps and voids (Figure 3a, yellow arrows), which is caused by elastic modulus differences of the LIC and S-NCM92.[27,28] After 100 cycles, aside from significant voids (Figure 3b, yellow arrows) between the cathode particles and the electrolyte arising from electrochemical side-reactions between S-NCM92 and LIC, internal cracks are generated due to the volume changes of S-NCM92 particles during cycling (Figure 3b, red arrows). These voids and cracks result in reduced dynamics with obstructed ion and electron conduction, further explaining why the $P_0F_0$ sample exhibits poor rate and cycle performance.
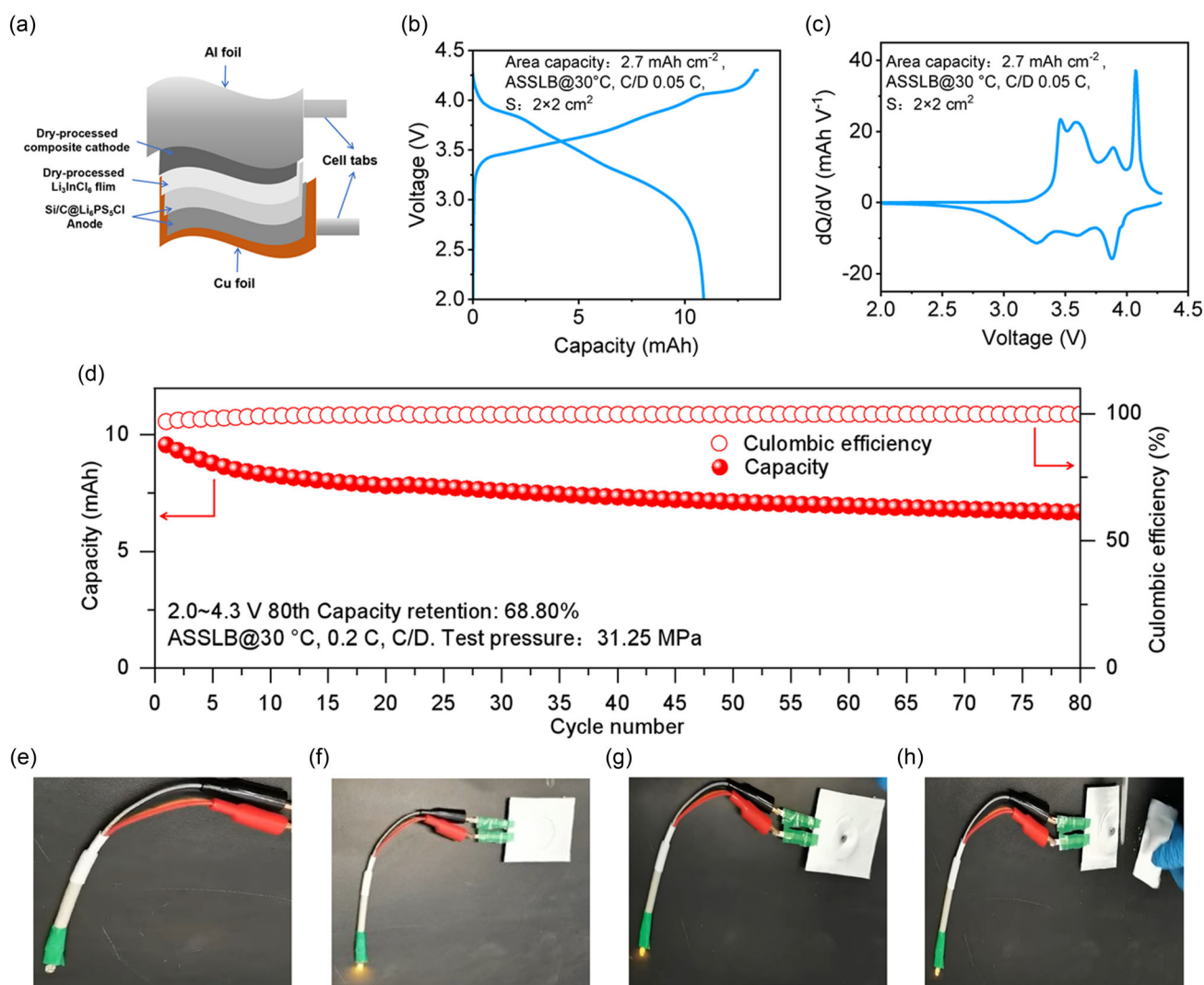


**Figure 4.** All solid-state pouch cell fabrication and performance evaluation. a) Schematic diagram of the layered all-solid-state pouch cell. b) Initial charge–discharge curve of the solid-state pouch cell. c) dQ/dV curve of the all-solid-state pouch cell for the first cycle. d) Cycling stability of the all-solid-state pouch cell. e) The photograph of an LED bulb in a non-operational state. f) The photograph of the all-solid-state pouch cell to power the LED bulb. g) The photograph of a solid-state pouch cell operating normally after puncture. h) The photograph of an all-solid-state pouch cell operating normally after cutting.

**Batteries & Supercaps**

Research Article
doi.org/10.1002/batt.202500375

**Chemistry Europe**
European Chemical
Societies Publishing

For the $P_0F_1$ sample, the initial contact between the components is significantly improved (Figure 3c), but the dispersion of a small amount of PTFE fibers in the composite cathode is uneven, leading to a lack of binder adhesion between the particles in some areas (Figure 3c yellow arrows), which is consistent with the characterization results in Figure 1e. Therefore, after 100 cycles, numerous gaps and internal cracks remain (Figure 3d, yellow and red arrows). In contrast, the self-lubricating and adhesive properties of PTFE particles improve the dispersion and cohesion between the particles of each component within the dry-processed composite cathode before and after 100 cycles (Figure 3e,f). We measured the thickness of the $P_0F_0$, $P_0F_1$, and $P_{1.5}F_1$ dry-processed composite cathodes under 400 MPa pressure, which show a decreasing trend (88, 65, and 59 μm, respectively, Figure 3g), accompanied by significantly increased compact density (2.31, 3.25, and 3.58 g cm$^{-3}$) and gradually decreased porosity[29] (38.73%, 15.14%, and 8.01%) (Figure 3h). These results further support the findings from the FIB-SEM characterizations (Figure 3a,c,e), ensuring more intimate contact between the components of the composite cathode and thereby enabling the excellent rate and cycle performance of the ASSLBs (Figure 2f,g).

The uniform distribution of elements such as Ni, Co, Mn, In, Cl, F, and C in Figure S4, Supporting Information confirms a uniform distribution of S-NCM92, VGCF, LIC, and particle-fiber PTFE within the $P_{1.5}F_1$ cathode. The potential of the dry-processed cathode on the current collector for large-scale applications is demonstrated (Figure S5, Supporting Information) by scaling up the area of the dry-film electrode to $130 \times 100$ mm$^2$ (Figure S6, Supporting Information). This fiber-particle composite binder strategy also suits the large-scale production of cathode electrodes for traditional lithium-ion batteries, thereby improving the film-formation quality of dry-processed composite cathodes.

Due to its best electrochemical performance, $P_{1.5}F_1$ was used to assemble an all-solid-state pouch cell, with N/P ratio of 1.1. The configuration of the pouch cell is shown in **Figure 4**a. The LIC layer was also prepared using a dry-processed technique with an area of $128 \times 98$ mm$^2$ (Figure S7a,b, Supporting Information) and a thickness of 70 μm (Figure S7c, Supporting Information), and a transfer printing technology was used to combine $Li_6PS_5Cl$ as a protective layer with a composite Si/C anode (Figure S8, Supporting Information). Electrochemical performance testing shows that at a current rate of 0.05 C the discharge capacity of the all-solid-state pouch cell is 10.89 mAh with an initial coulombic efficiency of 81.1% (Figure 4b). The dQ/dV curve of the pouch cell (Figure 4c) displays distinct peaks corresponding to the three-phase transitions of S-NCM92, consistent with the result in Figure 2c, indicating that the active material behaves normally. Cycling test of the all-solid-state pouch cell demonstrated a capacity retention rate of 68.8% after 80 cycles at 0.2 C (Figure 4d). The charge–discharge curves and dQ/dV curves show good overlap during the first three cycles, indicating sufficient reversibility of S-NCM92. However, as cycling progresses, the overlap diminishes and polarization increases, which may result from contact loss inside the pouch cell without high external pressure (Figure S9a–b, Supporting Information). Figure 4e shows the non-operational state of the LED bulb.

The all-solid-state pouch cell successfully powers an LED bulb (Figure 4f) and continues to operate normally even during puncturing (Figure 4g) and cutting (Figure 4h) tests, suggesting the great reliability and stability of the all-solid-state pouch cell benefiting from high-quality cathode film with fiber-particle composite binder.

## 3. Conclusion

In summary, we demonstrate that incorporation of 1.5 wt% particulate and 1 wt% fibrous PTFE as composite binder could significantly enhance film-forming quality of the composite cathodes. This improvement enables the continuous fabrication of high-quality, large-size dry-processed cathode films with better rate performance and cycling stability. A pouch cell integrating the optimized dry-processed ultrahigh nickel with a silicon-carbon composite anode delivers a discharge capacity of 10.89 mAh and an initial efficiency of 81.1%. Notably, the cell maintains electrochemical functionality after mechanical damage such as puncturing and cutting, successfully powering an LED bulb. These results highlight the fiber-particle composite binder as a promising strategy to improve the quality and processability of dry-processed composite cathodes, thereby advancing the practical deployment of durable ASSLBs.

## 4. Experimental Section

### Preparation of Dry-Processed Cathode Films

To prepare the dry-processed cathode films, we measured specific quantities of S-NCM92 ($D_{50} \approx 4$ μm, XTC), $Li_3InCl_6$ ($D_{50} \approx 5$ μm, KJ GROUP), VGCF, PTFE particles, and PTFE fibers ($M_w \approx 10^4$, DAIKIN), and put them into a mortar. The mass ratios were 70:30:1:x:1, with the values of × of 0 and 1.5, respectively. The materials were sequentially added to a mortar and thoroughly mixed. The resulting composite materials were then subjected to multiple compression cycles using a roller press at 75 °C to form dry-processed cathode films.

### Measurement of Ionic and Electronic Conductivities in Dry-Processed Composite Cathodes

The ionic and electronic conductivities of the dry-processed composite cathodes were measured using direct current (DC) polarization, with two symmetric cell configurations designed to isolate each transport mechanism. For electronic conductivity, a three-layer ion-blocking cell (Steel|$P_0F_1$ or $P_{1.5}F_1$ membrane|Steel) was assembled by pressing the composite membrane between two stainless-steel plungers at 400 MPa for 5 min to prevent ionic conduction. For ionic conductivity, a five-layer electron-blocking cell (InLi|$Li_6PS_5Cl$-LIC|$P_0F_1$ or $P_{1.5}F_1$ membrane|$Li_6PS_5Cl$-LIC|InLi) was used. The composite membrane was first pressed at 400 MPa, then 150 mg of $Li_6PS_5Cl$-LIC powder was applied to both sides and compressed under the same pressure, followed by placement of indium-lithium alloy electrodes at both ends. During testing, a constant DC voltage of 100 mV and an external pressure of 100 MPa were applied, and the resulting steady-state current was recorded to evaluate the respective conductivity. Values of ionic and electronic conductivity (σ) were calculated based on the following equation:

**Batteries & Supercaps**

Research Article
doi.org/10.1002/batt.202500375

Chemistry
Europe

European Chemical
Societies Publishing

$$\sigma = \frac{D \cdot I}{U \cdot S} \tag{1}$$

where $D$, $U$, $I$, and $S$ represent the thickness of the composite cathode layer (cm), the applied DC voltage (V), the steady-state current (A), and the effective area of the composite cathode (cm$^2$), respectively.

## Assembly of Mold Cells

The structure of the mold cell consisted of two stainless-steel electrodes and a PEEK (polyether ether ketone) sleeve. All electrode materials were placed within the PEEK sleeve. The mass of the samples taken from $P_0F_0$ (prepared by the powder pressing method, the composition of this composite cathode includes S-NCM92: LIC:VGCF=70:30:1), $P_0F_1$, and $P_{1.5}F_1$ were 16.5 mg, 16.6 mg, and 16.6 mg, respectively, which served as the cathode layers for the mold cells. For the second layer, 100 mg of $Li_3InCl_6$ powder was used, while for the third layer, 50 mg of $Li_6PS_5Cl$ powder was used. These layers were pressed at a pressure of 400 MPa maintaining for 5 min to form the solid electrolyte layers of the mold cell. The fourth layer, an InLi alloy, was then adhered to $Li_6PS_5Cl$ layer and pressed at 100 MPa. The testing temperature was set at 30 °C, with a voltage window of 2.6 ~ 4.3 V versus Li$^+$/Li. The electrochemical performance of the all-solid-state mold cell was tested under a pressure of 100 MPa.

## Porosity Calculation of Composite Cathodes

The porosity ($\varepsilon$) of the composite cathodes was calculated using the following equation:

$$\varepsilon = 1 - \frac{\rho_{compacted}}{\rho_{composite}} \tag{2}$$

where: $\rho_{compacted}$ represents the actual density of the composite cathode film with the unit expressed in g cm$^{-3}$. The actual density was determined by measuring the mass and volume of the fabricated composite cathode film. $\rho_{composite}$ is the theoretical density of the composite cathode, calculated using the following equation:

$$\rho_{composite} = \frac{1}{\frac{\omega_{S-NCM92}}{\rho_{S-NCM92}} + \frac{\omega_{LLZTC}}{\rho_{LLZTC}} + \frac{\omega_{PTFE}}{\rho_{PTFE}} + \frac{\omega_{VGCF}}{\rho_{VGCF}}} \tag{3}$$

where: $\omega_{S-NCM92}$, $\omega_{LIC}$, $\omega_{PTFE}$, $\omega_{VGCF}$ are the mass fractions of each component in the composite cathode. $\rho_{S-NCM92}$, $\rho_{LIC}$, $\rho_{PTFE}$, $\rho_{VGCF}$ are the respective densities of the components. All units are expressed in g cm$^{-3}$.

## Preparation of Dry-Processed $Li_3InCl_6$ Solid Electrolyte Membrane

To prepare the dry-processed $Li_3InCl_6$ solid electrolyte membrane, $Li_3InCl_6$ solid electrolyte powder and PTFE fibers were first weighed at a mass ratio of 99:1. The materials were thoroughly mixed and dispersed using a pestle in a mortar. Subsequently, the mixture was repeatedly pressed at 70 °C using a roller press to form a solid electrolyte membrane, with a membrane thickness of ≈70 μm. Finally, the resulting membrane was cut into dimensions of 20 × 20 mm$^2$ using a pneumatic punching machine for the assembly of pouch cells.

## Preparation of $Li_6PS_5Cl$ Solid Electrolyte Membrane

To prepare the $Li_6PS_5Cl$ solid electrolyte membrane, $Li_6PS_5Cl$ solid electrolyte powder (D$_{50}$ ≈ 5 μm) and nitrile butadiene rubber (NBR, M$_w$ ≈ 3800, Sigma Aldrich) binder were weighed using an electronic balance at a mass ratio of 97:3. The weighed materials were thoroughly mixed with xylene solvent using a planetary centrifugal mixer to form a uniform slurry. The prepared slurry was then coated onto a polyethylene terephthalate (PET) film. Subsequently, the coated PET film was placed in a vacuum drying oven and dried at 60 °C for 24 h. This process resulted in the fabrication of the $Li_6PS_5Cl$ solid electrolyte membrane with PET film substrate.

## Preparation of Composite Si/C Anode

To prepare the composite Si/C anode, Si powder (D$_{50}$ ≈ 1 μm), graphite powder (D$_{50}$ ≈ 10 μm) and poly(vinylidene fluoride) (PVDF, Kynar 761 A, M$_w$ ≈ 600) binder were weighed at a mass ratio of 7:3:0.1. Then N-methylpyrrolidone (NMP, 99%) solvent were added to the mixture. The components were thoroughly mixed using a planetary centrifugal mixer to form a uniform slurry. The resulting anode slurry was then coated onto a copper foil. The coated copper foil was transferred to a vacuum drying oven and dried at 60 °C for 12 h. This process produced the composite Si/C anode film.

## Preparation of the Transferred Anode

To prepare the transferred anode, the previously prepared $Li_6PS_5Cl$ solid electrolyte membrane was laminated onto the Si/C anode using a roller press to ensure proper adhesion between the $Li_6PS_5Cl$ film and the Si/C anode surface, followed by removal of PET film substrate. The resultant laminated anode was then cut into specific dimensions of 20 × 20 mm$^2$ using a pneumatic punching machine, making it suitable for pouch cell fabrication.

## Fabrication of All-Solid-State Pouch Cells

The cathode was prepared from the dry-processed electrode film ($P_{1.5}F_1$) and cut to dimensions of 20 × 20 mm$^2$ using a pneumatic punching machine, with an areal capacity of 2.7 mAh cm$^{-2}$. The transferred anode, $Li_3InCl_6$ solid electrolyte film, and the cathode film were stacked and pressed together at 600 MPa for 5 min to form the pouch cell. The assembled cells were then subjected to electrochemical performance testing under a constant pressure of 31.25 MPa (calculated using the parameters: T = 25 N·m, d = 0.01 m, A = 4 × 10$^{-4}$ m$^2$).

## Method for Estimating Pressure from Applied Torque

When a torque $T$ is applied to a bolt or clamp mechanism, it can be approximated as converting into a preload force F acting along the bolt axis. This force, when distributed over a known contact area $A$, yields a corresponding pressure $P$. The relationship is particularly useful for estimating mechanical stress conditions in experiments involving solid-state battery or similar compressed devices. A commonly used engineering approximation relates torque $T$ to preload force F via:

$$T \approx 0.2 \times F \times d \tag{4}$$

where $d$ is the nominal diameter of the bolt or the effective lever arm of the fastening mechanism, and the coefficient 0.2 is a typical empirical factor accounting for friction and thread geometry. The generated pressure $P$ over an area A is then:

$$P = \frac{F}{A} = \frac{T}{0.2 \times d \times A} \tag{5}$$

Units and Conversions Torque $T$: Expressed in N·m. Diameter $d$: Expressed in meters (m). Area $A$: Expressed in square meters (m$^2$). Force F: Calculated in Newtons (N). Pressure $P$: Resulting in Pascal (Pa). For convenience, 1 MPa = 10$^6$ Pa.

## Conflict of Interest

The authors declare no conflict of interest.

## Data Availability Statement

The data that support the findings of this study are available from the corresponding author upon reasonable request.

[1] Y. Anil Kumar, N. Roy, T. Ramachandran, M. A. Assiri, S. Srinivasa Rao, M. Moniruzzaman, S. W. Joo, *Dalton Trans.* **2024**, *53*, 12410.

[2] N. Sarfraz, N. Kanwal, M. Ali, K. Ali, A. Hasnain, M. Ashraf, M. Ayaz, J. Ifthikar, S. Ali, A. Hendi, N. Baig, M. F. Ehsan, S. S. Shah, R. Khan, I. Khan, *Energy Storage Mater.* **2024**, *71*, 103619.

[3] L. Ma, Y. Dong, N. Li, W. Yan, S. Ma, Y. Fang, Y. Li, L. Xu, C. Liu, S. Chen, R. Feng, L. Chen, D. Cao, Y. Lu, Q. Huang, Y. Su, F. Wu, *eTransportation* **2024**, *20*, 100.

[4] Y. Pang, J. Pan, J. Yang, S. Zheng, C. Wang, *Electrochem. Energy Rev.* **2021**, *4*, 169.

[5] Q. Wu, J. P. Zheng, M. Hendrickson, E. J. Plichta, *MRS Adv.* **2019**, *4*, 857.

[6] J. Yang, Z. Cao, Y. Chen, X. Liu, Y. Xiang, Y. Yuan, C. Xin, Y. Xia, S. Huang, Z. Qiang, K. K. Fu, J. Zhang, *ACS Nano* **2023**, *17*, 19903.

[7] J. Liu, B. Ludwig, Y. Liu, Z. Zheng, F. Wang, M. Tang, J. Wang, J. Wang, H. Pan, Y. Wang, *Adv. Mater. Technol.* **2017**, *2*, 1700106.

[8] Y. Han, S. H. Jung, S. Kwak, S. Jun, H. H. Kwak, J. H. Lee, S. T. Hong, Y. S. Jung, *Adv. Energy Mater.* **2021**, *11*, 2100126.

[9] K. Tuo, C. Sun, S. Liu, *Electrochem. Energy Rev.* **2023**, *6*, 17.

[10] B. Tao, D. Zhong, H. Li, G. Wang, H. Chang, *Chem. Sci.* **2023**, *14*, 8693.

[11] Y. Tanaka, K. Ueno, K. Mizuno, K. Takeuchi, T. Asano, A. Sakai, *Angew. Chem. Int. Ed.* **2023**, *62*, e202217581.

[12] S. Wang, Q. Bai, A. M. Nolan, Y. Liu, S. Gong, Q. Sun, Y. Mo, *Angew. Chem. Int. Ed.* **2019**, *58*, 8039.

[13] Y. C. Yin, J. T. Yang, J. D. Luo, G. X. Lu, Z. Huang, J. P. Wang, P. Li, F. Li, Y. C. Wu, T. Tian, Y. F. Meng, H. S. Mo, Y. H. Song, J. N. Yang, L. Z. Feng, T. Ma, W. Wen, K. Gong, L. J. Wang, H. X. Ju, Y. Xiao, Z. Li, X. Tao, H. B. Yao, *Nature* **2023**, *616*, 77.

[14] R. Li, P. Lu, X. Liang, L. Liu, M. Avdeev, Z. Deng, S. Li, K. Xu, J. Feng, R. Si, F. Wu, Z. Zhang, Y.-S. Hu, *ACS Energy Lett.* **2024**, *9*, 1043.

[15] Y.-C. Wu, F. Li, X. Cheng, Y. Tan, X. Huang, J.-D. Luo, S. Chen, R. Pan, Y.-C. Yin, Z. Liang, *Nano Lett.* **2024**, *24*, 15540.

[16] F. Li, X. Cheng, G. Lu, Y.-C. Yin, Y.-C. Wu, R. Pan, J.-D. Luo, F. Huang, L.-Z. Feng, L.-L. Lu, *J. Am. Chem. Soc.* **2023**, *145*, 27774.

[17] Y. J. Nam, D. Y. Oh, S. H. Jung, Y. S. Jung, *J. Power Sources* **2018**, *375*, 93.

[18] S. Wang, J. Liang, S. Li, H. Liang, X. Liu, Z. Liu, X. Xu, J. Lin, Y. Cui, T. Zhai, *Energy Storage Mater.* **2024**, *72*, 103726.

[19] S. Wang, X. Xu, C. Cui, C. Zeng, J. Liang, J. Fu, R. Zhang, T. Zhai, H. Li, *Adv. Funct. Mater.* **2022**, *32*, 2108805.

[20] W. Li, J. Liang, M. Li, K. R. Adair, X. Li, Y. Hu, Q. Xiao, R. Feng, R. Li, L. Zhang, S. Lu, H. Huang, S. Zhao, T.-K. Sham, X. Sun, *Chem. Mater.* **2020**, *32*, 7019.

[21] C. Wang, R. Yu, H. Duan, Q. Lu, Q. Li, K. R. Adair, D. Bao, Y. Liu, R. Yang, J. Wang, *ACS Energy Lett.* **2022**, *7*, 410.

[22] K. Lee, Y. Jo, J. Seok Nam, H. Yu, Y.-J. Kim, *Chem. Eng. J.* **2024**, *487*, 150221.

[23] K. J. Park, H. G. Jung, L. Y. Kuo, P. Kaghazchi, C. S. Yoon, Y. K. Sun, *Adv. Energy Mater.* **2018**, *8*, 1801202.

[24] Y. Li, C. Kim, E. Williams, Y. Su, J. Nanda, G. Yang, *Energy Environ. Mater.* **2025**, *8*, e12858.

[25] F. Li, Y.-C. Wu, X.-B. Cheng, Y. Tan, J.-D. Luo, R. Pan, T. Ma, L.-L. Lu, X. Wen, Z. Liang, *Energy Environ. Sci.* **2024**, *17*, 4187.

[26] W. Kim, J. Noh, S. Lee, K. Yoon, S. Han, S. Yu, K. H. Ko, K. Kang, *Adv. Mater.* **2023**, *35*, 2301631.

[27] S. Hao, Q. Zhang, X. Kong, Z. Wang, X. P. Gao, P. R. Shearing, *Adv. Energy Mater.* **2025**, *15*, 2404384.

[28] J. C. Stallard, L. Wheatcroft, S. G. Booth, R. Boston, S. A. Corr, M. F. L. De Volder, B. J. Inkson, N. A. Fleck, *Joule* **2022**, *6*, 984.

[29] W. Jiang, X. Zhu, R. Huang, S. Zhao, X. Fan, M. Ling, C. Liang, L. Wang, *Adv. Energy Mater.* **2022**, *12*, 2103473.